National Institute of Standards and Technology
Technology Administration, U.S. Department of Commerce

*NIST Technical Note 1535*

# Uncertainty of the NIST Electrooptic Sampling System

Dylan Williams
Paul Hale
Tracy Clement
Chih-Ming Wang

*NIST Technical Note 1535*

# Uncertainty of the NIST Electrooptic Sampling System

Dylan Willams
*Electromagnetics Division*

Paul Hale and Tracy Clement
*Optoelectronics Division*

Chih-Ming Wang
*Statistical Engineering Division*

National Institute of Standards and Technology
Boulder, CO 80305

December 2004

**U.S. Department of Commerce**
*Donald L. Evans, Secretary*

**Technology Administration**
*Phillip J. Bond, Under Secretary for Technology*

**National Institute of Standards and Technology**
*Hratch G. Semerjian, Acting Director*

Certain commercial entities, equipment, or materials may be identified in this document in order to describe an experimental procedure or concept adequately. Such identification is not intended to imply recommendation or endorsement by the National Institute of Standards and Technology, nor is it intended to imply that the entities, materials, or equipment are necessarily the best available for the purpose.

**National Institute of Standards and Technology Technical Note 1535**
**Natl. Inst. Stand. Technol. Tech. Note 1535, 32 pages (December 2004)**
**CODEN: NTNOEF**

U.S. GOVERNMENT PRINTING OFFICE
WASHINGTON: 2004

For sale by the Superintendent of Documents, U.S. Government Printing Office
Internet: bookstore.gpo.gov Phone: (202) 512-1800 Fax: (202) 512-2250
Mail: Stop SSOP, Washington, DC 20402-0001

# Uncertainty of the NIST Electrooptic Sampling System

Dylan Williams
Electromagnetics Division

Paul Hale and Tracy Clement
Optoelectronics Division

Chih-Ming Wang
Statistical Engineering Division

National Institute of Standards and Technology

We analyze the uncertainty of NIST's electrooptic sampling system. The system measures voltage waveforms in a coplanar waveguide fabricated on an electrooptic $LiTaO_3$ wafer. We use the system to measure the voltage waveform injected by a photodetector through a microwave probe into this coplanar waveguide. We then determine the voltage the photodetector would supply to a 50 Ω load at its coaxial connector. We calculate this voltage using an electrical mismatch correction that accounts for the effects of the probe and coplanar waveguide on the measured waveform.

Keywords: electrical phase; electrooptic sampling; mismatch correction; photodetector calibration; photodiode calibration.

## 1. Introduction

We present an uncertainty analysis for measurements performed with the NIST electrooptic sampling (EOS) system described in Refs. [1] and [2]. The EOS system measures the voltage waveform injected by a photodetector into a coplanar waveguide (CPW) fabricated on an electrooptic $LiTaO_3$ wafer. During post processing, we take a Fourier transform of the temporal waveform measured in the CPW. Using the mismatch corrections described in Ref. [1], we then determine the magnitude and phase of the frequency response of the voltage the photodetector would deliver to a 50 Ω load at its coaxial port.

We currently perform two types of measurements on the EOS system: measurements of photodetectors provided by customers and measurements of our own check standards. When we measure a customer's photodetector, we report the mean of $n_r = 3$ measurements. When we report a measurement of our check standard, we average $n_R$ sets of three measurements. In some cases, these additional measurements will reduce our measurement uncertainties significantly. Some customers use the NIST check standard to calibrate their instruments directly.

In the following, we separately estimate systematic type-B and statistically derived type-A uncertainties [3]. We also separately estimate the components of our type-A uncertainty due to

repeatability within each set of $n_r = 3$ measurements, and the long-term reproducibility between sets of three measurements. We also use a magnitude/phase representation for the data, rather than a real/imaginary representation. This is reasonable because the magnitude is much larger than the square root of its variance $s_m$, and the variance $s_\theta$ of the phase is small. Also, throughout the analysis we treat the magnitude and phase separately.

### 1.1 Check-standard Uncertainty

We report the mean of $n_R$ sets of $n_r = 3$ measurements when characterizing the check standard. To estimate the component of our type-A uncertainty in these measurements due to short-term repeatability, we average the $n_R$ variances from each set of measurements. We also separately estimate the component due to long-term reproducibility using a variance-component model. Finally, we use a Monte-Carlo simulator to estimate the uncertainty in the measurement due to systematic errors, which in our case are all of type B.

### 1.2 Uncertainty in Measurements of a Customer-supplied Photodetector

To estimate the component of the type-A uncertainty in the measurements of a customer's photodetector due to short-term repeatability, we perform each measurement of the photodetector's frequency response three times ($n_r = 3$). We perform only three measurements because each measurement takes approximately 100 hours to perform, and time constraints limit us to three repeat measurements per photodetector.

We report the mean of these three measurements of the magnitude and phase of the photodetector's frequency response when characterizing a customer's photodetector. We rely on our check-standard measurements to estimate the component of our type-A uncertainty in our measurements due to long-term reproducibility. Finally, we use a Monte-Carlo simulator to estimate the uncertainty in the measurement due to systematic errors.

### 1.3 Overview of the Uncertainty Analysis

For both our customer and check-standard measurements, we combine the repeatability, reproducibility, and systematic components of uncertainty to estimate the combined uncertainty and confidence intervals for our measurements. Throughout, we add a subscript 'r' to quantities associated with components of uncertainty due to imperfect short-term repeatability of measurements within a single set, a subscript 'R' to quantities associated with the component of our uncertainty due to imperfect long-term reproducibility between sets, and a subscript 's' to quantities associated with our type-B uncertainties caused by the systematic errors we identified. Due to the small number of measurements we perform, we do not estimate the correlation between the magnitude and phase measurements.

We combine these uncertainties following the recommendations of Ref. [3] in four consecutive steps. These are:

(1) Calculate the sample variances $s^2$ of the systematic (type-B), repeatability (type-A), and long-term reproducibility (type-A) errors separately.[1]
(2) Estimate the standard uncertainties $u$ in either the quantity of interest or its mean, as appropriate, from these variances.[2]
(3) Calculate the combined uncertainty from the sum of squares of the standard uncertainties associated with the systematic, repeatability, and reproducibility errors. The square of the combined uncertainty is an estimate of the variance of the averaged magnitude and phase responses we report.
(4) Estimate the coverage factor $k_{95}$ and expanded uncertainty $U$ corresponding to 95 % confidence intervals for the means we report from the combined uncertainty and the number of degrees of freedom $\nu$ associated with each of the standard uncertainties $u$. The number of degrees of freedom $\nu$ reflects the confidence we have in the standard uncertainties we use to form the combined uncertainty. The coverage factor $k_{95}$ is the factor by which we must multiply the combined uncertainty to form the expanded uncertainty $U$ and 95 % confidence intervals. The coverage factor $k_{95}$ depends on the number of effective degrees of freedom $\nu_{eff}$, which in turn depends on both the relative sizes of each component of the combined uncertainty and the number of degrees of freedom of each component.

## 2. Uncertainty due to Systematic Sources of Error

We estimate our systematic errors in the three magnitude-response measurements $m_i$ and the three phase-response measurements $\theta_i$ of the customer's photodetector with a Monte-Carlo simulator. For each of the three measurements, we run our Monte-Carlo simulator first with no errors, then $n_s = 100$ additional times with the systematic errors detailed in the rest of this report added into the measurements. At each frequency point we calculate the 100 magnitude and phase responses of the photodetector in the presence of the simulated errors. Finally, using $n_s = 100$, we determine the sample variances $s_{s,mi}^2$ and $s_{s,\theta i}^2$ of the 100 simulated values of the magnitude and phase for each of the three measurements $m_i$ and $\theta_i$.[1] These variances estimate the standard uncertainty in the $m_i$ and $\theta_i$ due to systematic sources that do not change from measurement to measurement, and are all of type B.

Since the sources of the systematic errors are similar in all of our measurements, and the measurements themselves are quite close, we have $s_{s,m1}^2 \approx s_{s,m2}^2 \approx s_{s,m3}^2$ and $s_{s,\theta 1}^2 \approx s_{s,\theta 2}^2 \approx s_{s,\theta 3}^2$. Thus we estimate our standard uncertainties $u_{s,\bar{m}}$ and $u_{s,\bar{\theta}}$ in the means $\bar{m}$ and $\bar{\theta}$ of the $m_i$ and $\theta_i$ due to

---

[1] We calculate sample variances $s$ from $s^2 = \frac{1}{n-1}\sum_i (y_i - \bar{y})^2$, where $n$ is the number of samples, the $y_i$ are the individual samples, and $\bar{y}$ is the mean of the $y_i$.

[2] We estimate the standard uncertainty of a quantity as $s$, the square root of its variance. We estimate uncertainty of means as $\sqrt{s^2/n}$, where $n$ is the number of samples. (Note that, since averaging more values increases confidence in a mean, the standard uncertainty of the mean of a quantity is smaller than $s$, the square root of the quantity's variance.).

these systematic sources of error from the average of the variances $s_{s,mi}^2$ and $s_{s,\theta i}^2$ using

$$u_{s,\bar{m}}^2 = \frac{\sum_{i=1}^{n_r} s_{s,mi}^2}{n_r} \quad \text{and} \quad u_{s,\bar{\theta}}^2 = \frac{\sum_{i=1}^{n_r} s_{s,\theta i}^2}{n_r}, \tag{1}$$

where $n_r$, the number of measurements, is equal to three. We assigned an infinite number of degrees of freedom $\nu_s$ to $u_{s,\bar{m}}$ and $u_{s,\bar{\theta}}$, as recommended in [3].

## 3. Variance due to Short-term Measurement Repeatability

The analysis of the random part of our uncertainty begins with an analysis of the component due to short-term measurement repeatability. To estimate our repeatability error within each set of three measurements, we estimate the sample variances $s_{r,m}^2$ and $s_{r,\theta}^2$ of the three measurements $m_i$ and $\theta_i$ using

$$s_{r,m}^2 = \frac{\sum_{i=1}^{n_r} (m_i - \bar{m})^2}{n_r - 1} \quad \text{and} \quad s_{r,\theta}^2 = \frac{\sum_{i=1}^{n_r} (\theta_i - \bar{\theta})^2}{n_r - 1}. \tag{2}$$

## 4. Variance due to Long-term Measurement Reproducibility

In addition to the short-term measurement repeatability within a set of three measurements discussed in the last section, our measurements within different sets may also differ due to long-term reproducibility. We also add the uncertainty due to long-term measurement reproducibility to our overall uncertainty. We determine the variances $\hat{s}_{R,\bar{m}}^2$ and $\hat{s}_{R,\bar{\theta}}^2$ characterizing the component of long-term reproducibility by repeating sets of three check-standard measurements. We do this using

$$\hat{s}_{R,\bar{m}}^2 = s_{R,\bar{m}}^2 - \frac{\bar{s}_{r,m}^2}{n_r} \quad \text{and} \quad \hat{s}_{R,\bar{\theta}}^2 = s_{R,\bar{\theta}}^2 - \frac{\bar{s}_{r,\theta}^2}{n_r}, \tag{3}$$

which separates out the components of varience $\bar{s}_{r,m}^2$ and $\bar{s}_{r,\theta}^2$ due to short-term measurement repeatability from the total variances $s_{R,\bar{m}}^2$ and $s_{R,\bar{\theta}}^2$ of the means of our sets of three measurements performed over a longer time span. We estimate the average sample variances $\bar{s}_{r,m}^2$ and $\bar{s}_{r,\theta}^2$ in Eq. **(3)** due to short-term repeatability error by averaging the $s_{r,m}^2$ and the $s_{r,\theta}^2$ over the $n_R$ sets of $n_r = 3$ measurements. If either $\hat{s}_{R,\bar{m}}^2$ or $\hat{s}_{R,\bar{\theta}}^2$ in Eq. **(3)** is negative, we set it to zero.

## 5. Combining Uncertainties

We estimate the combined uncertainties $u_{\bar{m}}$ and $u_{\bar{\theta}}$ of $\bar{m}$ and $\bar{\theta}$ from the long-term reproducibility components $u_{R,\bar{m}}$ and $u_{R,\bar{\theta}}$ of uncertainty, the short-term repeatability components $u_{r,\bar{m}}$ and $u_{r,\bar{\theta}}$ of uncertainty, and the systematic components $u_{s,\bar{m}}$ and $u_{s,\bar{\theta}}$ of uncertainty using

$$u_{\bar{m}}^2 = u_{R,\bar{m}}^2 + u_{r,\bar{m}}^2 + u_{s,\bar{m}}^2 \quad \text{and} \quad u_{\bar{\theta}}^2 = u_{R,\bar{\theta}}^2 + u_{r,\bar{\theta}}^2 + u_{s,\bar{\theta}}^2 \ . \tag{4}$$

Thus the combined uncertainties $u_{\bar{m}}$ and $u_{\bar{\theta}}$ include both measurement repeatability, reproducibility, and systematic sources of uncertainty: they represent our best estimate of the standard uncertainty of our results. The values of $u_{s,\bar{m}}$ and $u_{s,\bar{\theta}}$ are determined by **(1)**. The values of $u_{R,\bar{m}}$, $u_{r,\bar{m}}$, $u_{R,\bar{\theta}}$, and $u_{r,\bar{\theta}}$ will be described below.

### 5.1. Customer Measurements

As we have only just recently finished our first long-term reproducibility study, for our customer measurements we have to date neglected $u_{R,\bar{m}}$ and $u_{R,\bar{\theta}}$ in Eq. **(4)**. When we are ready to include $u_{R,\bar{m}}$ and $u_{R,\bar{\theta}}$ in Eq. **(4)**, we will determine them from our check-standard measurements with

$$u_{R,\bar{m}}^2 = \hat{s}_{R,m}^2 \quad \text{and} \quad u_{R,\bar{\theta}}^2 = \hat{s}_{R,\theta}^2 \ . \tag{5}$$

The number of degrees of freedom $\nu_R$ associated with $u_{R,\bar{m}}$ and $u_{R,\bar{\theta}}$ is $n_R - 1$. For customer measurements, we determine the standard uncertainties $u_{r,\bar{m}}$ and $u_{r,\bar{\theta}}$ from

$$u_{r,\bar{m}}^2 = \frac{s_{r,m}^2}{n_r} \quad \text{and} \quad u_{r,\bar{\theta}}^2 = \frac{s_{r,\theta}^2}{n_r} \ , \tag{6}$$

where $n_r$, the number of measurements used to form the mean, is equal to three. The number of degrees of freedom $\nu_r$ associated with $u_{r,\bar{m}}$ and $u_{r,\bar{\theta}}$ is $n_r - 1$.

### 5.2. Check-standard Measurements

Since we average $n_R$ measurements to characterize our check-standards, we do not use **(5)** and **(6)** to determine the uncertainties in Eq. **(4)**. For our check-standard measurements, we determine the standard uncertainties $u_{R,\bar{m}}$ and $u_{R,\bar{\theta}}$ due to long-term measurement reproducibility with

$$u^2_{R,\bar{m}} = \frac{\hat{s}^2_{R,m}}{n_R} \quad \text{and} \quad u^2_{R,\bar{\theta}} = \frac{\hat{s}^2_{R,\theta}}{n_R} \; . \tag{7}$$

Again, the number of degrees of freedom $\nu_R$ associated with $u_{R,\bar{m}}$ and $u_{R,\bar{\theta}}$ is $n_R - 1$. Since for our check standard we report a mean of a number of measurement sets, we assign our short-term uncertainty with

$$u^2_{r,\bar{m}} = \frac{\bar{s}^2_{r,m}}{n_R \; n_r} \quad \text{and} \quad u^2_{r,\bar{\theta}} = \frac{\bar{s}^2_{r,\theta}}{n_R \; n_r} \; , \tag{8}$$

rather than with **(6)**. Here the number of degrees of freedom $\nu_r$ associated with $u_{r,\bar{m}}$ and $u_{r,\bar{\theta}}$ is $n_R \, (n_r - 1)$.

## 6. Expanded Uncertainty and 95 % Confidence Intervals

To determine our expanded uncertainties $U_{95,\bar{m}}$ and $U_{95,\bar{\theta}}$ corresponding to 95 % confidence intervals for $\bar{m}$ and $\bar{\theta}$, we must take into account our relative confidence in the standard uncertainties $u_{s,\bar{m}}$, $u_{s,\bar{\theta}}$ , $u_{r,\bar{m}}$ and $u_{r,\bar{\theta}}$. This requires determining the "coverage factor" $k_{95}$ [3] from the combined uncertainties $u_{\bar{m}}$ and $u_{\bar{\theta}}$.

We determine $k_{95}$ from $\nu_{eff}$, the effective number of degrees of freedom in the measurements. We determine $\nu_{eff}$ from estimates of the number of degrees of freedom $\nu_s$ of our systematic errors and the number of degrees of freedom $\nu_r$ and $\nu_R$ of our repeatability and reproducibility with the Welch-Satterthwaite formula

$$\nu_{eff,\bar{m}} = \frac{u^4_{\bar{m}}}{\dfrac{u^4_{R,\bar{m}}}{\nu_R} + \dfrac{u^4_{r,\bar{m}}}{\nu_r} + \dfrac{u^4_{s,\bar{m}}}{\nu_s}} \tag{9}$$

and

$$\nu_{eff,\bar{\theta}} = \frac{u^4_{\bar{\theta}}}{\dfrac{u^4_{R,\bar{\theta}}}{\nu_R} + \dfrac{u^4_{r,\bar{\theta}}}{\nu_r} + \dfrac{u^4_{s,\bar{\theta}}}{\nu_s}} \; , \tag{10}$$

as recommended in Appendix B.3 of Ref. [3]. We calculate our coverage factors $k_{95}$ from $k_{95} = t_{95}(\nu_{eff})$, where $t_{95}(\nu_{eff})$ is the two-sided 95$^{th}$ percentile of Student's $t$-distribution with $\nu_{eff}$ degrees of freedom. Finally, we determine our expanded uncertainties of $\bar{m}$ and $\bar{\theta}$ from $U_{95,\bar{m}} = k_{95,\bar{m}} u_{\bar{m}}$ and

Figure 1. Representative measurement of a check-standard voltage spectral density.

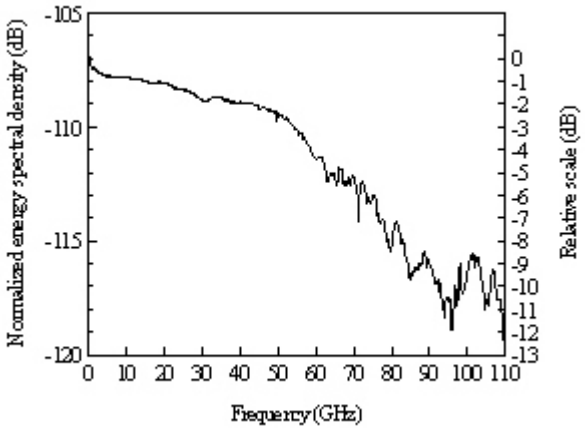


Figure 2. Normalized energy spectral density corresponding to the voltage of Fig. 1.

$U_{95,\bar{\theta}} = k_{95,\bar{\theta}} u_{\bar{\theta}}$. There is a 95 % confidence that the true values of $\bar{m}$ and $\bar{\theta}$ lie within the expanded uncertainty intervals $\bar{m} \pm U_{95,\bar{m}}$ and $\bar{\theta} \pm U_{95,\bar{\theta}}$.

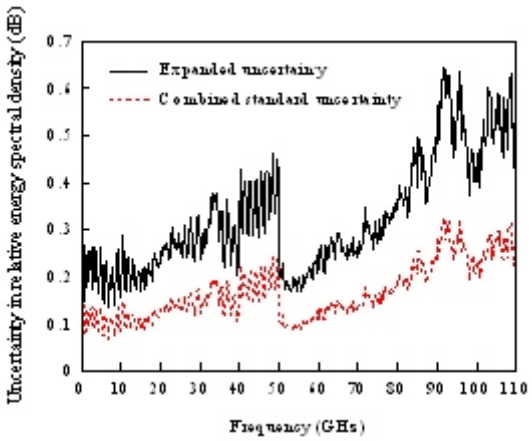


Figure 3. Representative uncertainty in our check-standard measurements of spectral density.

## 7. Representative Measurement Result

From each measurement on the electrooptic sampling system we form both an absolute and a relative voltage magnitude response of the photodetector, and a linearized phase response. We represent the absolute voltage response of the photodetector as the spectral density of the voltage generated by the detector normalized to the charge drawn by the detector when it is excited by a narrow optical pulse. This spectral density has units of V/C·Hz, and corresponds to the voltage output that the detector would generate across a 50 Ω load connected at its coaxial output port over a bandwidth of one hertz after being excited by an optical impulse that drew one coulomb of charge through the photodetector's electrical bias port. This is useful because we can better measure the bias current generated by the photodetector in response to an optical impulse than determine the power in each optical impulse. Figure 1 shows a representative measurement of the spectral density of a detector's voltage response.

We report our measurements on a 200 MHz grid to 110 GHz. We extract these measurements from a time record that is only about 2 ns long, which we pad to 5 ns before calculating the Fourier transforms. Because the time record is short, measured results represent average values over a bandwidth of roughly 500 MHz. Furthermore, small voltage offsets in the temporal measurements manifest themselves as energy between DC and 500 MHz. We have not yet fully characterized or

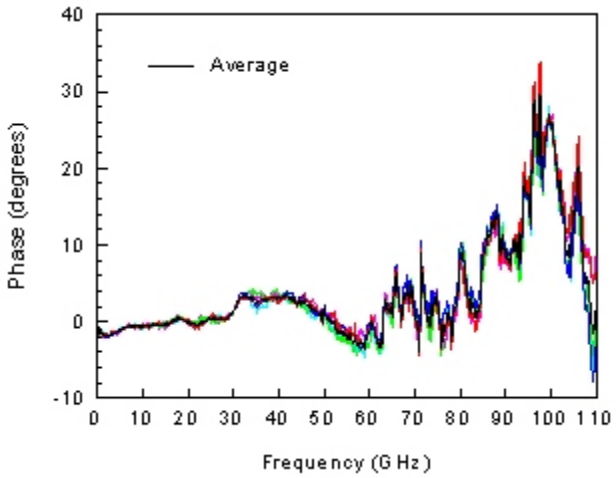


Figure 4. Comparison of five check-standard phase measurements.

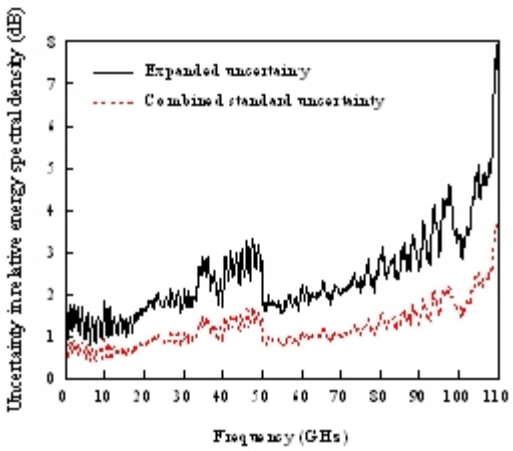


Figure. 5. Representative uncertainty in our check-standard measurements of phase.

developed methods to eliminate these small offsets, so our measurements and error estimates may not reliably reflect the actual distribution of power below about 500 MHz.

We also measure a normalized version of the voltage spectral density. The quantity we determine from each measurement is the energy that the photodetector generates in a 50 Ω load in a 1 hertz bandwidth normalized to the total energy we measure from the detector over our total measurement bandwidth (usually 110 GHz). Figure 2 shows the normalized energy density corresponding to the measurement in Fig. 1 expressed in decibels. The values plotted in the figure are on the order of $10^{-11}$ because the energy in a 1 Hz bandwidth is small compared to the total energy in the 110 GHz spectrum we measure. The relative scale on the right facilitates determining quantities such as the detector's 3 dB bandwidth; Fig. 3 shows the associated uncertainty in the measurement.

We also measure the relative phase response of the detectors. We report the phase of the voltage the detector will generate across a 50 Ω load after subtracting a time delay from the phase response that minimizes the measured phase below 30 GHz in the least-squares sense. Figure 4 shows the measured phase response of one of our check standards. It compares 5 sets of three measurements to the mean of these five sets of measurements.

We report the standard and expanded uncertainty for each measurement as well. Figure 5 plots the uncertainty in phase for the check-standard measurements presented in Fig. 4. For this measurement, which is an average of the mean of five measurement sets, the systematic errors dominate. Keep in mind that these results are only representative. Not only will results vary from photodetector to photodetector, but the uncertainties we achieve depend on experimental conditions and may change from measurement to measurement. Furthermore, we are not able to characterize the response of a customer's photodetector with the same accuracy as our check standard, because we are unable to perform more than three measurements on each customer's photodetector.

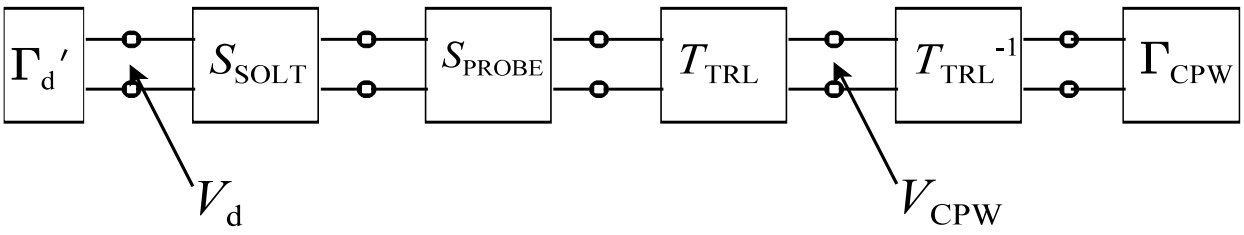


$$T_{\mathrm{TRL}} \equiv T_{\Gamma}\ \mathrm{T}(S_{\mathrm{l}})\ \mathrm{T}(S_{\mathrm{m}}')\ \mathrm{T}(S_{\mathrm{m}}'')\ \mathrm{T}(\Delta S')$$

Figure 6. The electrical model used to represent the errors in the electrooptic sampling system.

## 8. Specific Forms Used to Represent Systematic Errors

In what follows, we derive the form of each component of systematic error we consider to determine the variances $s_{\mathrm{s},\mathrm{m}i}^2$ and $s_{\mathrm{s},\theta i}^2$. These error mechanisms can be divided into two categories, those having to do with the mismatch correction (SOLT calibration errors, reflection coefficient measurement errors, and on-wafer scattering parameter measurement errors) and those having to do with the finite impulse response of the EOS system itself. We model most of the errors having to do with the mismatch corrections as two-port electrical circuit elements in the electrical circuits between the photodetector and the on-wafer reference plane. We model the errors having to do with the finite impulse response of the EOS system as multiplicative errors in the frequency domain.

Figure 6 shows the electrical model we use to represent the errors due to imperfect mismatch corrections in the electrooptic sampling system. The voltage $V_{\mathrm{d}}$ represents the voltage across the detector, and the voltage $V_{\mathrm{CPW}}$ represents the voltage that the electrooptic sampling system measures in the coplanar waveguide (CPW) transmission line. Parameters denoted by a $\Gamma$ represent reflection coefficients, those by an $S$ represent scattering-parameter matrices, and those by a $T$ represent cascade matrices. The function T($S$) in the equation embedded in the figure represents the cascade matrix corresponding to its argument, which is a scattering-parameter matrix $S$. $\Gamma_{\mathrm{d}}'$ represents the reflection coefficient of the detector and its measurement errors (see section 8.4.2), $S_{\mathrm{SOLT}}$ the errors in the coaxial SOLT calibration, $T_{\mathrm{TRL}}$ the errors in the on-wafer TRL calibration in the coplanar waveguide transmission lines, and $\Gamma_{\mathrm{CPW}}$ the reflection coefficient of the CPW resistor. The quantities $T_{\Gamma}$, $S_{\mathrm{l}}$, $S_{\mathrm{m}}'$, $S_{\mathrm{m}}''$, and $\Delta S'$ represent errors in the on-wafer TRL calibration, and are discussed in detail later.

The equations in the rest of this document describe in greater detail how we add systematic errors into the Monte-Carlo simulations we use to determine the variances $s_{\mathrm{s},\mathrm{m}i}^2$ and $s_{\mathrm{s},\theta i}^2$. We use the symbol $\mu$ to denote random variables with a zero mean and Gaussian distribution having a variance of 1. Using this notation, we would use $m + \sigma\mu$ to represent a random variable having a Gaussian distribution with mean $m$ and variance $\sigma^2$ (i.e., a Gaussian distribution having mean $m$ and standard

deviation σ).

The symbol μ with no argument denotes a single variable chosen once randomly during each iteration of the Monte-Carlo simulator. The symbol μ(*f*) denotes a variable chosen randomly during each iteration at each frequency *f*. No μ in any equation is correlated to any other μ in any other equation. When we use more than one random variable within the same equation, we add subscripts to the symbol μ to explicitly show which μ are the same and which are uncorrelated.

We use the symbol η in a fashion analogous to the use of the symbol μ to describe errors uniformly distributed over the range [−1,1]. We use these uniformly distributed errors to account for worst-case error limits. As a general rule, after we correct for a systematic error δ, we then add errors in the simulations that are uniformly distributed over the range [−δ/2,δ/2] to account for the uncertainty in the correction we have applied. We use smaller ranges in the simulator only if we are able to present arguments that the uncertainty in our estimate of the systematic errors is smaller than [−δ/2,δ/2]. We believe that in most cases this a conservative estimate of the uncertainty in the correction.

## 8.1 On-wafer TRL Scattering Parameter Calibration

These errors are represented as transmission matrices that we cascade onto the right-hand side of the scattering parameters of the probe head. We also cascade them onto the left-hand side of our measurements of the CPW resistors that we use to terminate the signal coming from the photodetector (see Fig. 6).

### 8.1.1 TRL Reference Impedance Offset (from Ref. [4])

The errors in determining the overall magnitude of the reference impedance of the TRL calibration are represented by the transmission matrix $T_\Gamma$, which is the cascade matrix of an ideal impedance transformer. $T_\Gamma$ is given by

$$T_\Gamma \equiv \frac{1}{\sqrt{1-\Delta\Gamma^2}} \begin{bmatrix} 1 & \Delta\Gamma \\ \Delta\Gamma & 1 \end{bmatrix}, \qquad \textbf{(11)}$$

where

$$\Delta\Gamma = \frac{1}{2}\left[\left(\frac{\Delta C}{C}\right)_c \eta_1 + \frac{\Delta L}{L}\eta_2 + \left(\frac{\Delta C}{C}\right)_w \eta_3 + \left(\frac{\Delta C}{C}\right)_{dc} \mu_4\right]. \qquad \textbf{(12)}$$

The component of the systematic error in the load method we use to calculate the capacitance of the CPW is the worst-case error

$$\left(\frac{\Delta C}{C}\right)_c = 0.01 \quad . \qquad \textbf{(13)}$$

The value in Eq. **(13)** was derived from Ref. [5], where we compared measurements of CPW capacitance performed by different methods.

The component due to CPW line-length variations is

$$\frac{\Delta L}{L} = \frac{1\ \mu\text{m}}{20\ \text{cm}} = 0.000005\ . \qquad \textbf{(14)}$$

We derived this from a worst-case variation in line-length of ±1 μm we expect on the masks and from the analysis presented in Ref. [4].

The component due to CPW line-width variations is

$$\left(\frac{\Delta C}{C}\right)_{\text{w}} = 0.024\ . \qquad \textbf{(15)}$$

We derived this from field calculations using the method of Ref. [6] assuming a ±1 μm error in linewidths on the CPW. This results in a 2 μm change in the gap, which corresponds to a change in capacitance of 2.4 %. These calculations are shown in Appendix 1.

We also add a component not discussed in Ref. [4] to Eq. **(12)** to account for errors in our on-wafer DC resistance measurements. That factor is

$$\left(\frac{\Delta C}{C}\right)_{\text{DC}} = \sqrt{2}\ \frac{\sigma_{\text{DC}}}{R_{\text{DC}}}\ , \qquad \textbf{(16)}$$

where $R_{\text{DC}}$ is the measured DC resistance of the CPW load used to determine the capacitance of the CPW line, and $\sigma_{\text{DC}}$ is our estimate of the standard deviation of the error in measuring that DC resistance. The square root of 2 is required in Eq. **(16)** because the difference of two resistance measurements determines the resistance of the load, a measurement of the DC resistance of an on-wafer short and a measurement of the DC resistance of an on-wafer load.

We found that our accuracy in measuring DC resistance depends on the quality of the contacts that the probe tips make with the CPW lines printed on the $LiTaO_3$ wafer, and degrades with the number of connections. For example, in one experiment, initial DC resistance measurements were repeatable to within about 0.01 Ω, but after 100 contacts on the same device, we measured a standard deviation of our on-wafer resistance measurements that increased to over 4 Ω. Thus, we estimate the standard deviation $\sigma_{\text{DC}}$ of our DC resistance measurements at the time at which we performed each calibration. To do this, we measure the DC resistance of each standard in both our initial and repeat measurements. Then, we estimate the standard deviation $\sigma_{\text{DC}}$ from the differences $\Delta R_i$ we measured under the assumption that the mean of the $\Delta R_i$ was 0. We use the formula

$$\sigma_{DC} = \sqrt{\frac{\sum_i \Delta R_i^2}{2\, n_{DC}}}\,, \tag{17}$$

where $n_{DC}$ is the number of measurements. The factor of 2 is required in **(17)** because the $\Delta R_i$ correspond to the difference of two resistance measurements, and we wish to estimate the error in a single resistance measurement.

### 8.1.2 TRL Reference-plane Position Error Due to Asymmetric CPW Short (from Ref. [4])

We represent the errors in the reference-plane position of the TRL calibration with the transmission matrix corresponding to the scattering matrix $S_1$, which is an approximation to the scattering matrix of an ideal reference plane shift. $S_1$ is given by

$$S_1 \equiv \begin{bmatrix} 0 & 1+i\delta \\ 1+i\delta & 0 \end{bmatrix}, \tag{18}$$

where

$$\delta = \frac{2\pi f}{c}\,(1\ \mu\text{m})\,\eta\,\sqrt{\frac{1+\epsilon_s}{2}}\,, \tag{19}$$

and where $\epsilon_s$, the approximate relative dielectric constant of the $LiTaO_3$ substrate at microwave frequencies, is 43. These expressions were derived from approximations in Ref. [4] and the assumption of an error of $\pm 1$ μm in the metal pattern on the wafer.

### 8.1.3 Metal Conductivity (from Ref. [4])

Variations in metal conductivity and thickness within a TRL calibration set also introduce errors into the calibration. We accounted for these errors with the simulator described in Ref. [4]. At each frequency, we used the simulator to generate the scattering parameter matrix $S_m$, which represents a worst-case error in the on-wafer TRL calibration due to variations in the resistance of the lines. As inputs to the program, we used an on-wafer scattering-parameter calibration performed in the lines and introduced a resistance perturbation in the longest line based on DC measurements of the resistances of the line. This introduces the greatest errors in the calibration [4].

Finally, we represent the errors in terms of a transmission matrix corresponding to the scattering parameter matrix $S_m'$ defined by

$$S_m' \equiv \begin{bmatrix} 0 & 1 \\ 1 & 0 \end{bmatrix} + \begin{bmatrix} S_{m11} & S_{m12}-1 \\ S_{m12}-1 & S_{m22} \end{bmatrix} \eta\ . \tag{20}$$

We correlate the errors in Eq. **(20)** because they have a single source, the resistance of the line.

### 8.1.4 Metal Conductivity Across the Wafer

Variations in metal conductivity and thickness across the wafer also introduce errors into the measurements. This occurs because the calibration is performed at a location with one value of metal conductivity and thickness, while the appropriate calibration requires that the metal conductivity and thickness be equal to that at the location at which the measurement was made. We account for these errors by performing two calibrations, one at the center of the wafer, where the lines are least resistive, and one at the edge of the wafer, where the lines are most resistive. Then we use the calibration comparison method of Ref. [7] to quantify the differences in the two calibrations.

We represented the errors in terms of a transmission matrix corresponding to the scattering parameter matrix $S_m''$ defined by

$$S_m'' \equiv \begin{bmatrix} 0 & 1 \\ 1 & 0 \end{bmatrix} + \begin{bmatrix} S_{m11}' & S_{m12}'-1 \\ S_{m12}'-1 & S_{m22}' \end{bmatrix} \eta \ . \qquad \textbf{(21)}$$

Here $S_m'$ was the scattering parameter matrix representing the differences between the two calibrations determined by the calibration comparison method. We correlate these errors because they have a single source, the local conductivity and/or thickness of the metal film. These errors were not considered in the analyses we performed before May 2004.

## 8.2 Drift Error Measured by the Calibration Comparison Method of Ref. [7]

To determine the scattering parameters of the probe head, we first performed a coaxial short-open-load-thru (SOLT) calibration. Then we performed two on-wafer TRL calibrations. We calculate the scattering parameters of the probe head from the first on-wafer calibration, and the drift in the measurement from the differences between the first and the second on-wafer calibration using the calibration comparison method described in Ref. [7]. Since these errors are generally due to only a few sources of drift in the analyzer, they are highly correlated. Using the same form as above, we represent the drift errors in terms of the transmission matrix corresponding to the worst-case drift errors from the scattering parameter matrix $\Delta S'$, where

$$\Delta S' \equiv \begin{bmatrix} 0 & 1 \\ 1 & 0 \end{bmatrix} + \begin{bmatrix} \Delta S_{11} & \Delta S_{12}-1 \\ \Delta S_{12}-1 & \Delta S_{22} \end{bmatrix} \eta \ . \qquad \textbf{(22)}$$

In **(22)**, $\Delta S$ is the scattering parameter matrix representing the worst-case error in the on-wafer TRL calibration due to test-set drift determined by the calibration comparison method.

### 8.3 Error in the DC Scattering Parameters

We also determine the scattering parameters of the probe head and the reflection coefficient of the CPW load from on-wafer DC resistance measurements. We add a resistance of $\mu_1\sigma_{DC}$ to our measurement of the DC resistance of the probe head and, since the resistance of the on-wafer CPW load is set to the difference of the measurement of the resistances of the load and a short, we add a resistance of $\sqrt{2}\ \mu_2\sigma_{dc}$ to the measured resistance of the CPW load.

### 8.4 Coaxial SOLT Scattering Parameter Calibration

In our early work, we tested photodetectors with 2.4 mm coaxial connectors. More recently, we have focused on testing high-bandwidth photodetectors with 1 mm coaxial connecters.

We estimate errors of the 40 GHz 2.4 mm coaxial SOLT calibrations used to characterize our photodetectors with 2.4 mm coaxial connectors with the "HP8510 Specifications and Performance Verification Analysis Software" [8], [9] provided by the manufacturer of the vector network analyzer and coaxial calibration kit used. We estimate errors in the 110 GHz 1 mm coaxial SOLT calibrations used to characterize high-bandwidth photodetectors with the "HP8510 Specifications and Performance Verification Analysis Software" [10].

The computer programs [8] and [10] do not supply information on how the errors of the SOLT calibrations are correlated with frequency, so we did not correlate the errors of the SOLT calibration with frequency. Thus, our Monte-Carlo simulations are most accurate when estimating the uncertainties of quantities determined one frequency at a time, such as the power spectral density generated by the detector or the absolute phase of its response. Because we do not calculate these correlations, the error analysis is not suitable for determining the temporal properties of the calibrated pulses.

In this program, we chose the parameters most applicable to our equipment and procedures. For our 2.4 mm calibrations, we specified the HP8516A test set, the HP834X016 source, the HP85056A calibration kit, and the sliding load calibration technique. Although we used cables from another manufacturer not supported in the error analysis software, we specified the HP 85133F pair of short cables because we felt that they corresponded most closely to the cables we used in our experiments.

The program generates tables of what we treat as $3\sigma$ errors for the frequency ranges 0.045 to 2 GHz, 2 to 20 GHz, 20 to 36 GHz, and 36 to 40 GHz. We generate our distributions of errors in our Monte-Carlo simulator based on the uncertainties in these tables. The decision to treat these errors in this way is based on conversations with Doug Rytting and Ken Wong of Hewlett-Packard. Doug and Ken were involved in the development of the software described in Refs. [8] and [10] and with unpublished work used to investigate the proper treatment of the quantities generated by Refs. [8] and [10]. The values drawn from Ref. [8] are summarized in Table 1. The quantities denoted with a prime in the table correspond to uncertainties in the characterization of the reflection coefficient of the detector, rather than the error boxes.

**Table 1.**
**2.4 mm connector 3-σ errors reported by [8]**

| | <2 GHz | 2-20 GHz | 20-36 GHz | > 36 GHz | Measurement Condition |
|---|---|---|---|---|---|
| $e_{11}$[a] | $8.998\times10^{-3}$ | $9.113\times10^{-3}$ | $1.6001\times10^{-2}$ | $1.6118\times10^{-2}$ | $\lvert S_{11}\rvert\approx\lvert S_{22}\rvert\approx0$, $\lvert S_{21}\rvert\approx\lvert S_{12}\rvert\approx0$ |
| $e_{22}$[b] | $1.717\times10^{-2}$ | $1.7594\times10^{-2}$ | $2.8513\times10^{-2}$ | $2.8631\times10^{-2}$ | $\lvert S_{11}\rvert\approx\lvert S_{22}\rvert\approx0$, $\lvert S_{21}\rvert\approx\lvert S_{12}\rvert\approx1$ |
| $e_{21}$[c] | $5.8\times10^{-3}$ | $7.2\times10^{-3}$ | $1.66\times10^{-2}$ | $1.76\times10^{-2}$ | $\lvert S_{11}\rvert\approx\lvert S_{22}\rvert\approx0$, $\lvert S_{21}\rvert\approx\lvert S_{12}\rvert\approx1$ |
| $e_{\phi21}$[d] | $7.9\times10^{-3}$ | $6.96\times10^{-2}$ | 0.127 | 0.14 | $\lvert S_{11}\rvert\approx\lvert S_{22}\rvert\approx0$, $\lvert S_{21}\rvert\approx\lvert S_{12}\rvert\approx1$ |
| $e_{11}'$[e] | $8.492\times10^{-3}$ | $8.952\times10^{-3}$ | $1.4017\times10^{-2}$ | $1.4058\times10^{-2}$ | HP83440D |
| $e_{\phi11}'$[f] | $1.92\times10^{-2}$ | $8.05\times10^{-2}$ | 0.1456 | 0.1678 | ($\lvert S_{22}\rvert\approx0$, $\lvert S_{21}\rvert\approx\lvert S_{12}\rvert\approx0$) |

[a] From table "S11 lower worst-case uncertainty specifications".

[b] From table "S22 lower worst-case uncertainty specifications".

[c] From table "S21 lower RSS uncertainty specifications". We take the table value $m$ in dB in the row corresponding to the level of $|S_{21}|$ equal to 0 dB and calculate $e_{21}$ from $1-10^{-m/20}$.

[d] From table "S21 lower RSS uncertainty specifications". We take the table value θ in degrees in the row corresponding to the level of $|S_{21}|$ equal to 0 dB and set $e_{\phi21}$ equal to sin(θ).

[e] From table "S11 lower RSS uncertainty specifications". We picked values in the rows corresponding to reflection coefficient $|S_{11}| = 0.5$ below 20 GHz, $|S_{11}| = 0.4$ from 20−36 GHz, and $|S_{11}| = 0.3$ from 36−40 GHz. Since the values of $e_{11}'$ and $e_{\phi11}'$ depend on the reflection coefficient of the detector, values used for other detectors may be different.

[f] Values correspond to preceding row, but we take the table value θ in degrees and set $e_{\phi11}$ equal to sin(θ).

We also chose parameters applicable to our equipment for our 110 GHz 1 mm coaxial SOLT calibrations. In the program [10] for the frequency range of 45 MHz to 50 GHz, we specified the HPE7342 test set, the HP8365xXF source, the HP85059A calibration kit, and the broadband load calibration technique. For the frequency range of 50 GHz to 110 GHz, we specified the HPE7352A110 test set, the HP836xxXF source, the HP85059A110 calibration kit, and the offset short calibration technique. We also specified the DIRECTXF test port cables (no cables) because no specification for 1 mm test cables was available in the analysis.

The program generated tables of what we treated as 3σ errors for the frequency ranges 2 to 18 GHz, 18 to 40 GHz, 40 to 50 GHz, 50 to 75 GHz, 75 to 85 GHz, 85 to 100 GHz, and 100 to 110 GHz. We generated our distributions of errors in the simulator based on the uncertainties in these tables. The values drawn from [10] are summarized in Tables 2 and 3. Here again, the quantities denoted with a prime in the tables correspond to uncertainties in the characterization of the reflection coefficient of the detector, rather than the error boxes. Since the program did not report errors below 2 GHz, we used the values reported by the program from 2 to 18 GHz below 2 GHz.

To account for the effects of bending on the cables, we measured the scattering parameters of a coaxial "thru" connection after each on-wafer experiment. Since we know that this thru connection is reciprocal, we averaged the phase of the forward and backward transmission coefficients, and fit the result to a line with an intercept at 0 to determine the phase slope $\zeta_i$ for each measurement. We then estimated the standard deviation $\sigma_\zeta$ of the phase slope under the assumption that the mean phase slope was 0. We used the formula

$$\sigma_\zeta = \sqrt{\frac{\sum_i \zeta_i^2}{2n_c}}, \tag{23}$$

where $n_c$ was the number of measurements. The factor of 2 in the denominator of Eq. **(23)** accounts for the fact that we measure the total phase change in the two cables, whereas the error in the measurement is caused by only the cables attached to the probe head we are characterizing.

**Table 2.**
**1 mm connector 3-σ errors reported in [10] for frequencies less than 50 GHz**

| | <2 GHz | 2-18 GHz | 18-40 GHz | 40-50 GHz | Measurement Condition |
|---|---|---|---|---|---|
| $e_{11}$ [a] | 0.032623 | 0.032623 | 0.051144 | 0.064121 | $\|S_{11}\|\approx\|S_{22}\|\approx 0$, $\|S_{21}\|\approx\|S_{12}\|\approx 0$ |
| $e_{22}$ [b] | 0.077705 | 0.077705 | 0.122345 | 0.153653 | $\|S_{11}\|\approx\|S_{22}\|\approx 0$, $\|S_{21}\|\approx\|S_{12}\|\approx 1$ |
| $e_{21}$ [c] | $3.235\times10^{-2}$ | $3.235\times10^{-2}$ | $5.118\times10^{-2}$ | $8.085\times10^{-2}$ | $\|S_{11}\|\approx\|S_{22}\|\approx 0$, $\|S_{21}\|\approx\|S_{12}\|\approx 1$ |
| $e_{\phi 21}$ [d] | $3.41\times10^{-2}$ | $3.41\times10^{-2}$ | $5.955\times10^{-2}$ | $9.1\times10^{-2}$ | $\|S_{11}\|\approx\|S_{22}\|\approx 0$, $\|S_{21}\|\approx\|S_{12}\|\approx 1$ |
| $e_{11}'$ [e] | $4.946\times10^{-2}$ | $3.9708\times10^{-2}$ | $6.3261\times10^{-2}$ | $6.8597\times10^{-2}$ | NEL detector |
| $e_{\phi 11}'$ [f] | $5.685\times10^{-2}$ | $5.863\times10^{-2}$ | $9.887\times10^{-2}$ | 0.1474 | ($\|S_{22}\|\approx 0$, $\|S_{21}\|\approx\|S_{12}\|\approx 0$) |
| $e_{11}'$ [g] | 0.031688 | 0.031688 | $5.0441\times10^{-2}$ | $6.3491\times10^{-2}$ | U2T detector T2.D25.515.B6.116 |
| $e_{\phi 11}'$ [f] | 0.3188 | 0.3188 | 0.2606 | 0.3273 | ($\|S_{22}\|\approx 0$, $\|S_{21}\|\approx\|S_{12}\|\approx 0$) |

[a] From table "S11 lower worst-case uncertainty specifications".

[b] From table "S22 lower worst-case uncertainty specifications".

[c] From table "S21 lower RSS uncertainty specifications". We take the table value $m$ in dB in the row corresponding to the level of $|S_{21}|$ equal to 0 dB and calculate $e_{21}$ from $1-10^{-m/20}$.

[d] From table "S21 lower RSS uncertainty specifications". We take the table value θ in degrees in the row corresponding to the level of $|S_{21}|$ equal to 0 dB and set $e_{\phi 21}$ equal to sin(θ).

[e] From table "S11 lower RSS uncertainty specifications" generated by [10]. We picked values in the rows corresponding to reflection coefficient $|S_{11}| = 0.9$ below 2 GHz, $|S_{11}| = 0.7$ from 2 to 40 GHz, $|S_{11}| = 0.5$ from 40 to 50 GHz, $|S_{11}| = 0.4$ from 50 to 85 GHz, and $|S_{11}| = 0.3$ from 85 to 110 GHz. Since the values of $e_{11}'$ and $e_{\phi 11}'$ depend on the reflection coefficient of the detector, values used for other detectors may be different.

[f] Values correspond to preceding row, but we take the table value θ in degrees and set $e_{\phi 11}$ equal to sin(θ).

[g] From table "S11 lower RSS uncertainty specifications" generated by [10]. We picked values in the rows corresponding to reflection coefficient $|S_{11}| = 0.1$ below 18 GHz, $|S_{11}| = 0.2$ from 18 to 50 GHz, $|S_{11}| = 0.5$ from 50 to 85 GHz, and $|S_{11}| = 0.8$ from 85 to 110 GHz. Since the values of $e_{11}'$ and $e_{\phi 11}'$ depend on the reflection coefficient of the detector, values used for other detectors may be different.

**Table 3.**
**1 mm connector 3-σ errors reported in [10] for frequencies greater than 50 GHz**

| | 50-75 GHz | 75-85 GHz | 85-100 GHz | 100-110 GHz | Measurement Condition |
|---|---|---|---|---|---|
| $e_{11}$[a] | 0.042998 | 0.043213 | 0.053521 | 0.053521 | $\|S_{11}\|\approx\|S_{22}\|\approx 0$, $\|S_{21}\|\approx\|S_{12}\|\approx 0$ |
| $e_{22}$[b] | 0.084111 | 0.084266 | 0.104882 | 0.104882 | $\|S_{11}\|\approx\|S_{22}\|\approx 0$, $\|S_{21}\|\approx\|S_{12}\|\approx 1$ |
| $e_{21}$[c] | $3.891\times10^{-2}$ | $4.343\times10^{-2}$ | $5.421\times10^{-2}$ | $5.421\times10^{-2}$ | $\|S_{11}\|\approx\|S_{22}\|\approx 0$, $\|S_{21}\|\approx\|S_{12}\|\approx 1$ |
| $e_{\phi 21}$[d] | $4.852\times10^{-2}$ | $5.924\times10^{-2}$ | $7.277\times10^{-2}$ | $7.451\times10^{-2}$ | $\|S_{11}\|\approx\|S_{22}\|\approx 0$, $\|S_{21}\|\approx\|S_{12}\|\approx 1$ |
| $e_{11}'$[e] | $4.306\times10^{-2}$ | $4.308\times10^{-2}$ | $5.1644\times10^{-2}$ | $5.1644\times10^{-2}$ | NEL detector |
| $e_{\phi 11}'$[f] | 0.1178 | 0.1239 | 0.1908 | 0.1926 | ($\|S_{22}\|\approx 0$, $\|S_{21}\|\approx\|S_{12}\|\approx 0$) |
| $e_{11}'$[g] | $4.511\times10^{-2}$ | $4.514\times10^{-2}$ | $6.6559\times10^{-2}$ | $6.6559\times10^{-2}$ | U2T detector T2.D25.515.B6.116 |
| $e_{\phi 11}'$[f] | 0.1003 | 0.1064 | 0.1019 | 0.1037 | ($\|S_{22}\|\approx 0$, $\|S_{21}\|\approx\|S_{12}\|\approx 0$) |

[a] From table "S11 lower worst-case uncertainty specifications".

[b] From table "S22 lower worst-case uncertainty specifications".

[c] From table "S21 lower RSS uncertainty specifications". We take the table value $m$ in dB in the row corresponding to the level of $|S_{21}|$ equal to 0 dB and calculate $e_{21}$ from $1-10^{-m/20}$.

[d] From table "S21 lower RSS uncertainty specifications". We take the table value θ in degrees in the row corresponding to the level of $|S_{21}|$ equal to 0 dB and set $e_{\phi 21}$ equal to sin(θ).

[e] From table "S11 lower RSS uncertainty specifications" generated by [10]. We picked values in the rows corresponding to reflection coefficient $|S_{11}| = 0.9$ below 2 GHz, $|S_{11}| = 0.7$ from 2 to 40 GHz, $|S_{11}| = 0.5$ from 40 to 50 GHz, $|S_{11}| = 0.4$ from 50 to 85 GHz, and $|S_{11}| = 0.3$ from 85 to 110 GHz. Since the values of $e_{11}'$ and $e_{\phi 11}'$ depend on the reflection coefficient of the detector, values used for other detectors may be different.

[f] Values correspond to preceding row, but we take the table value θ in degrees and set $e_{\phi 11}$ equal to sin(θ).

[g] From table "S11 lower RSS uncertainty specifications" generated by [10]. We picked values in the rows corresponding to reflection coefficient $|S_{11}| = 0.1$ below 18 GHz, $|S_{11}| = 0.2$ from 18 to 50 GHz, $|S_{11}| = 0.5$ from 50 to 85 GHz, and $|S_{11}| = 0.8$ from 85 to 110 GHz. Since the values of $e_{11}'$ and $e_{\phi 11}'$ depend on the reflection coefficient of the detector, values used for other detectors may be different.

### 8.4.1 Probe-head Characterization

We incorporated the effect of the coaxial SOLT calibration on the scattering parameters of the probe head by cascading the transmission matrix corresponding to $S_{SOLT}$ on the left side of the probe head. We developed expressions for the matrix based on the relations (26) to (29) in Ref. [11] between the 12-term and 8-term error model. We determined $S_{SOLT}$ from

$$S_{SOLT} \equiv \begin{bmatrix} \frac{e_{11}}{3.41}(\mu_1(f)+i\mu_2(f)) & \sqrt{1+\frac{e_{21}}{3}\mu_3(f)+i\frac{e_{\phi 21}}{3}\mu_4(f)+if\sigma_\zeta\mu_7} \\ \sqrt{1+\frac{e_{21}}{3}\mu_3(f)+i\frac{e_{\phi 21}}{3}\mu_4(f)+if\sigma_\zeta\mu_7} & \frac{\sqrt{e_{22}^{\,2}-e_{11}^{\,2}}}{3.41}(\mu_5(f)+i\mu_6(f)) \end{bmatrix} \quad \textbf{.(24)}$$

In Eq. **(24)** the factors of 3 in the off-diagonal terms convert the 3-σ limits from [8] and [10] and summarized in Tables 1, 2, and 3 into 1-σ values. The square roots in the off-diagonal terms account for the fact that the transmission errors from the SOLT calibration are evenly distributed between the error boxes of the probe we are trying to characterize on port 1 of the network analyzer and the error box of the second probe on port two of the network analyzer. The two off-diagonal terms are equal because the 2-tier algorithm we use forces the forward and reverse transmission coefficients to be equal, which is justified based on reciprocity arguments.

We determined the first diagonal term in Eq. **(24)** from the values of $e_{11}$ in the tables, the uncertainties in measuring reflection coefficients under the conditions $|S_{11}| \approx 0$ and $|S_{21}| = 0$. The error in the measurement of the reflection coefficient $S_{11}$ is equal to the first diagonal term in Eq. **(24)**.

Under the conditions $|S_{11}| \approx |S_{22}| \approx 0$ and $|S_{21}| \approx |S_{21}| \approx 1$, the total error described by $e_{22}$ in the measurement of the reflection coefficient $S_{22}$ has two major components. The first is the error described by $e_{11}$ due to the finite port match on port 2, and the second is due to the second diagonal term in Eq. **(24)**. Thus we subtracted in a root-mean-square sense the partial error $e_{11}$ we were not interested in from the total error $e_{22}$ to arrive at the second diagonal term in Eq. **(24)** we were trying to determine. We used the assumption that the two error sources were uncorrelated to arrive at this expression.

Finally, the factor of 3.41 in the diagonal elements in Eq. **(24)** convert the 3-σ magnitude limit $R$ from [8] and the table into 1-σ values for the real and imaginary part of the reflection coefficients. To arrive at the factor of 3.41, we assumed Gaussian distributions in $x$ and $y$ with variance σ. This results in a Gaussian distribution in magnitude $r$ with no angular dependence. We then integrated this magnitude distribution over a disk of radius $R$, and arrive at the 99.7 percentile point for $R$ = 3.41 σ. The calculations are outlined in Appendix 2.

### 8.4.2 Photodetector Reflection Coefficient

Because the detector has a large reflection coefficient at its coaxial port, we treated the magnitude errors described by $e_{11}'$ and the phase errors described by $e_{\phi 11}'$ separately. In the simulations we determined the reflection coefficient $\Gamma_d'$ at the coaxial port of the photodetector by perturbing the nominal value of $\Gamma_d$ with

$$\Gamma_d' \equiv \Gamma_d + \frac{\Gamma_d}{|\Gamma_d|}\left[\frac{e_{11}'}{3}\mu_1(f) + i\frac{e_{\phi 11}'}{3}\mu_2(f)\right]. \qquad \textbf{(25)}$$

In Eq. **(25)** the factors of 3 convert the 3-σ limits from [8] as summarized in the tables into 1-σ values. The factor of $\Gamma_d/|\Gamma_d|$ ensures that the magnitude errors described by $e_{11}'$ change the magnitude of $\Gamma_d$ and the phase errors described by $e_{\phi 11}'$ change the phase of $\Gamma_d$.

In order to avoid damaging the detectors with our ohmmeter, we estimated the DC reflection coefficient of the detector from the low-frequency limit of its reflection coefficient $\Gamma_d'$.

## 8.5 Finite Impulse Response of the Electro-optic Sampling System

The impulse response of the electrooptic sampling system is broadened by several distinct physical mechanisms [2]. Thus the measured voltage waveform on the CPW wafer is a convolution of the actual voltage present there and the finite impulse response of the electrooptic sampling system. This convolution in the time domain can be represented as a multiplication in the frequency domain, which is how we choose to treat these errors. This section describes how we accounted for these systematic errors, which we discussed in greater detail in Ref. [2], in our simulations.

### 8.5.1 Optical Reflection from the Back Surface of the $LiTaO_3$ Wafer

A small portion of the optical sampling beam bounces off of the back side of the wafer, returns to the surface where it re-samples the electrical signal, and then re-reflects to the detectors. We used the analysis described in Ref. [2] to estimate the worst-case magnitude error $E_r$ in decibels and the phase error $\theta_r$ in degrees of the measurement system at each frequency due to the first three optical round-trip reflections in the wafer.

To perform the calculations, we assumed that the anti-reflective coating on the back of the wafer reflected 0.05 % of the incident optical power. This worst-case estimate was based on a reflectance curve supplied by the manufacturer of the wafer, and a measurement we performed of the spectrum of the optical beam, which showed that the optical power was concentrated between 1500 nm and 1600 nm. These measurements and the curve from the manufacturer are shown in Appendix 3. We calculated the reflection coefficient of the front surface of the wafer from the index of refraction $n$ of the $LiTaO_3$, for which we used a value of 2.12 [12].

We do not know if the optical reflections in the wafer add or subtract from the magnitude and phase

of the final result, so we did not correct for for this systematic error. However, we expect these errors to be correlated, so the simulator adds random magnitude errors $\eta E_r$ to the magnitude calculation, which was expressed in decibels, and random phase errors $\eta \theta_r$ to the phase calculation, which was expressed in degrees to account for the uncertainty of the measurements.

### 8.5.2 Radius of the Optical Beam Traversing the Wafer

We focus the optical sampling beam to a small spot on the wafer. The finite radius of the spot broadens the measured pulse slightly. We used the analysis introduced in Ref. [13], which assumes a lowest-order cylindrical Gaussian mode of radius $r$, to estimate the error in the magnitude response of the electrooptic sampling system.

We first estimated that the radius of the spot was about 3 μm at the surface of the wafer by passing the beam through small holes in the metallization on the wafer.

By Gaussian optics, we estimated the radius $r$ of the beam in the substrate as $r(z) = r(0)\,(1 + (z/z_r)^2)^{1/2}$, where $z$ is the depth in the substrate, $z_r = \pi\,(r(0))^2\,n/\lambda$, $n = 2.12$ is the index of refraction of the $LiTaO_3$, and $\lambda$, the optical wavelength, is about 1550 nm. Under the assumption that $r(0)$ is equal to 3 μm, the calculation predicts a beam radius $r' \equiv r(35\ \mu m) = 4\ \mu m$ at a point 35 μm into the substrate, which corresponds roughly to the 50 % point of the electric field in the substrate.

Based on these estimates, we adopted a correction for our magnitude response due to an error $E_w$ calculated using formula (10) in Ref. [13] with $r' = 4$ μm, our best estimate of the average beam radius in the substrate. (Note that the authors of Ref. [13] use $w$ to express the radius of the beam rather than $r'$.) We expressed the correction in decibels. We also added random errors $\frac{1}{2}\eta E_w$ to the magnitude calculation, which was also expressed in decibels.

### 8.5.3 Finite Temporal Width of the Optical Pulses Measured by the Autocorrelator

The shape and temporal width of the optical pulses emanating from the laser do not affect the phase response of the measurement system, but do lower its magnitude response. We used optical autocorrelator measurements to correct for this systematic measurement error.

To estimate these errors, we took a direct Fourier transform of the autocorrelator measurements. After determining the error $E_a$ in our autocorrelator measurements, we corrected our magnitude response by $E_a$ decibels to account for this systematic error. Finally, the simulator added random magnitude errors of $\frac{1}{2}\eta E_a$ to the magnitude calculation, which was also expressed in decibels, to account for the uncertainty in our correction.

### 8.5.4 Finite Time the Optical Pulses Spend Traversing the Electric Field of the CPW Mode

The optical pulses spend a finite time traversing the electric field of the coplanar waveguide, which penetrates below the surface of the $LiTaO_3$ wafer. As discussed in Ref. [13], this not only broadens the impulse response of the measurement system, but shifts its phase response.

To correct for this systematic measurement error, we performed calculations of the electric-field profile in the substrate with the full-wave simulator described in Ref. [14]. We used 315 modes in the electromagnetic calculation, but found that reducing the number of modes to half that many resulted in no discernable difference in the calculations. From this experiment, we concluded that the calculation method, at least, did not introduce significant errors into the estimation of the errors.

The ±2 μm worst-case width error we expect in the 40 μm gap of the CPW will introduce a ± 2 μm/40 μm, or ±5 %, error in our estimate of the extent to which the fields penetrate into the substrate. Calculations of the correction as a function of substrate thickness showed that a ± 25 μm error in the substrate thickness leads to a negligible ±0.02 % deviation in magnitude and an even smaller ±0.002 % deviation in phase.

However, the anisotropic permitivity is a significant source of error that we did not attempt to account for. The relative dielectric constant in the propagation direction ($x$) and into the substrate ($y$) is about 43, while the relative dielectric constant in the $z$ direction transverse to the propagation direction and parallel to the substrate surface is about 53 [12]. The method of Ref. [14] cannot account for anisotropic dielectric constant, but we expect that the unequal dielectric constants in the $y$ and $z$ directions will distort the fields by an amount roughly equal to the change in the dielectric constant in the two directions, or about 26 %. So we estimated that our worst case error in the overall estimate was ±0.26, and note that our uncertainty in this correction could be reduced significantly if we were to use an electromagnetic field simulator that could account correctly for the anisotropic substrate dielectric constant.

After calculating the magnitude error $E_{CPW}$ in decibels and phase error $\theta_{CPW}$ in degrees from the field calculations based on the method of Ref. [14] and the formulas in Ref. [13], we corrected both our magnitude and phase responses to account for this systematic error. Finally, we added random magnitude errors of $0.26\,\eta\,E_{CPW}$ to the magnitude calculation, which was expressed in decibels, and random phase errors of $0.26\,\eta\,\theta_{CPW}$ to the phase calculation, which was expressed in degrees. Here we left these two errors completely correlated, as we would expect them to be in practice.

---

The authors thank Robert Judish for his clear and thoughtful explanations of the statistical principles and analysis employed in this work, and Doug Rytting and Ken Wong for their explanations of the HP SOLT error analysis software.

## 9. References


[1] D.F. Williams, P.D. Hale, T.S. Clement, and J.M. Morgan, "Mismatch corrections for electro-optic sampling systems," *56th ARFTG Conf. Dig.*, pp. 141-145, Nov. 30-Dec. 1, 2000.

[2] D.F. Williams, P.D. Hale, T.S. Clement, and J.M. Morgan, "Calibrating electro-optic sampling systems," *Int. Microwave Symp. Dig.*, Phoenix, AZ, pp. 1527-1530, May 20-25, 2001.

[3] B.N. Taylor and C.E. Kuyatt, "Guidelines for evaluating and expressing the uncertainty of NIST measurement results," NIST Technical Note 1297, 1994 edition.

[4] R.F. Kaiser and D.F. Williams, "Sources of Error in Coplanar-Waveguide TRL Calibrations," *54th ARFTG Conf. Dig.*, pp. 75-80, Dec. 1-2, 1999.

[5] D. F. Williams and R. B. Marks, "Transmission Line Capacitance Measurement," *IEEE Microwave Guided Wave Lett.*, vol. 1, no. 9, pp. 243-245, Sept. 1991.

[6] W. Heinrich, "Quasi-TEM Description of MMIC Coplanar Line Including Conductor-Loss Effects," *IEEE Trans. Microwave Theory Tech.* 41, pp. 45-52, January 1993.

[7] D. F. Williams, R. B. Marks, and A. Davidson, "Comparison of On-Wafer Calibrations," *38th ARFTG Conf. Dig.*, pp. 68-81, Dec. 1991.

[8] "HP8510 Specifications and Performance Verification Analysis Software," Hewlett-Packard part number 08510-10033, Program revision A.04.00, Data revision A.04.00.

[9] The National Institute of Standards and Technology does not endorse commercial products. Similar instruments or products may work as well or better.

[10] "HP8510 Specifications and Performance Verification Analysis Software," Hewlett-Packard part number 08510-10033, Program revision A.05.00, Data revision A.05.00.

[11] R.B. Marks, "Formulations of the basic vector network analyzer error model including switch terms," *50th ARFTG Conf. Dig.*, pp. 115-126, Dec. 1997.

[12] "Optical Crystals," data sheet from Crystal Technology (A Siemens Company), 1035 East Meadow Circle, Palo Alto, California, 94303.

[13] B.H. Kolner and D.M. Bloom, "Electrooptic sampling in GaAs integrated circuits," *IEEE J. Quantum Electron.*, vol. QE-22, no. 1, pp. 79-93, Jan.1986.

[14] W. Heinrich, "Full-wave analysis of conductor losses on MMIC transmission lines," *IEEE Trans. Microwave Theory Tech.*, vol. 38, no. 10, pp. 1468-1472, Oct. 1990.

## Appendix 1.

A summary of calculations found in page 136 of Dylan Williams' laboratory notebook #4. A change of ±1 μm in a metal edge changes the gap width from 40 μm to 38 μm, yielding the 24 % relative change in capacitance.

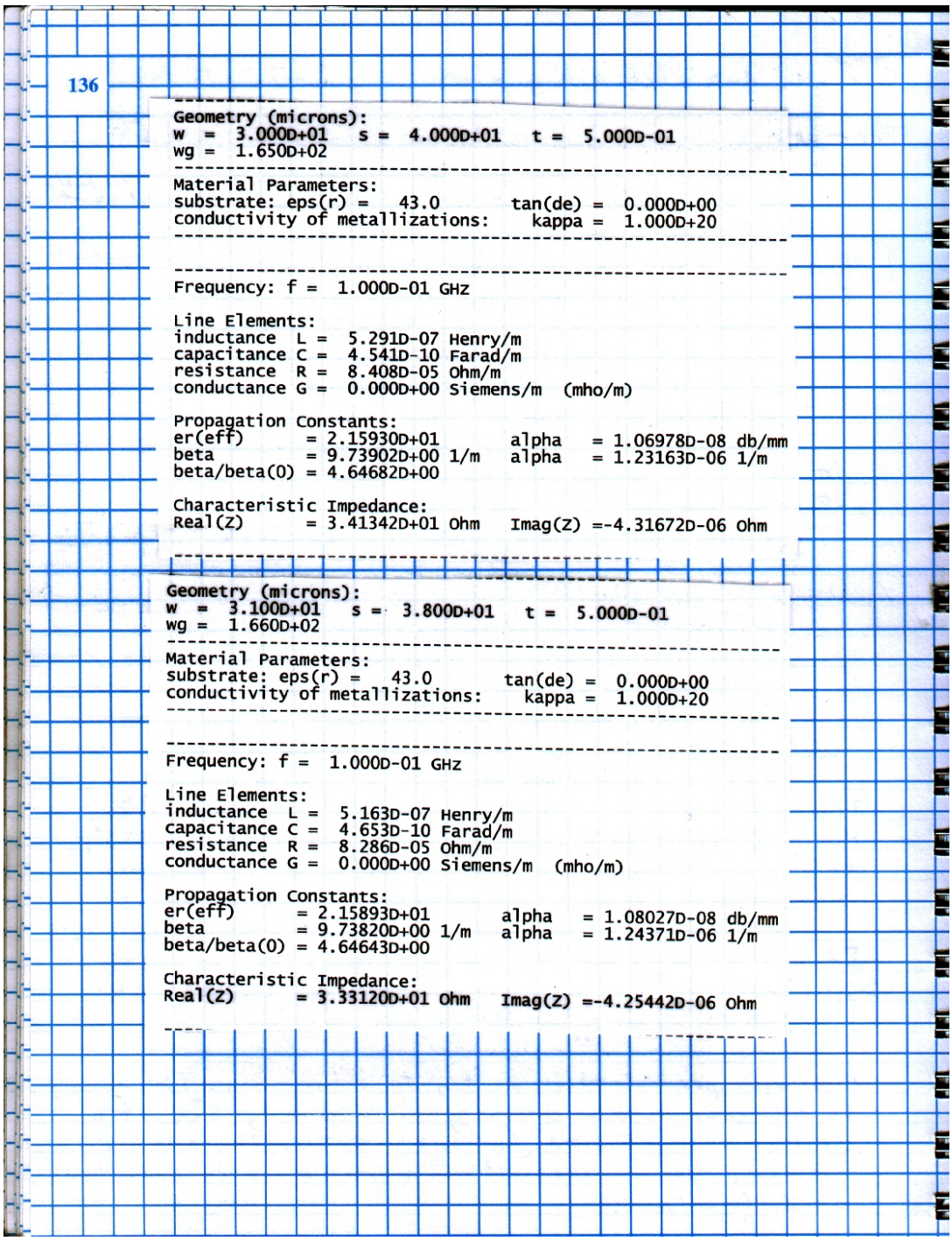

136

Geometry (microns):
w = 3.000D+01 s = 4.000D+01 t = 5.000D-01
wg = 1.650D+02

Material Parameters:
substrate: eps(r) = 43.0 tan(de) = 0.000D+00
conductivity of metallizations: kappa = 1.000D+20

Frequency: f = 1.000D-01 GHz

Line Elements:
inductance L = 5.291D-07 Henry/m
capacitance C = 4.541D-10 Farad/m
resistance R = 8.408D-05 Ohm/m
conductance G = 0.000D+00 Siemens/m (mho/m)

Propagation Constants:
er(eff) = 2.15930D+01 alpha = 1.06978D-08 db/mm
beta = 9.73902D+00 1/m alpha = 1.23163D-06 1/m
beta/beta(0) = 4.64682D+00

Characteristic Impedance:
Real(Z) = 3.41342D+01 Ohm Imag(Z) =-4.31672D-06 Ohm

Geometry (microns):
w = 3.100D+01 s = 3.800D+01 t = 5.000D-01
wg = 1.660D+02

Material Parameters:
substrate: eps(r) = 43.0 tan(de) = 0.000D+00
conductivity of metallizations: kappa = 1.000D+20

Frequency: f = 1.000D-01 GHz

Line Elements:
inductance L = 5.163D-07 Henry/m
capacitance C = 4.653D-10 Farad/m
resistance R = 8.286D-05 Ohm/m
conductance G = 0.000D+00 Siemens/m (mho/m)

Propagation Constants:
er(eff) = 2.15893D+01 alpha = 1.08027D-08 db/mm
beta = 9.73820D+00 1/m alpha = 1.24371D-06 1/m
beta/beta(0) = 4.64643D+00

Characteristic Impedance:
Real(Z) = 3.33120D+01 Ohm Imag(Z) =-4.25442D-06 Ohm

## Appendix 2.

We develop the factor of 3.41 in the diagonal elements in Eq. **(24)** that convert the 3-σ magnitude limit $R$ from [8] and the table into 1-σ values for the real and imaginary part of the reflection coefficients. To arrive at the factor of 3.41, we assumed Gaussian distributions in $x$ and $y$ with variance σ=1 with functional form

$$f(x,y) = \frac{1}{2\pi} e^{-x^2/2} e^{-y^2/2} = \frac{1}{2\pi} e^{-r^2/2}, \qquad \textbf{(26)}$$

where $f$ is the distribution of errors, $x$ and $y$ correspond to the real and imaginary coordinates, $r$ corresponds to the distance from the origin. If $F(R)$ if the probability that $f$ is inside a disk of radius $R$,

$$F(R) = \int_0^R \int_0^{2\pi} f(r)\, d\theta\, r\, dr = \int_0^R e^{-r^2/2}\, d\left(\frac{r^2}{2}\right) = 1 - e^{-R^2/2} \equiv z, \qquad \textbf{(27)}$$

where $R = \sqrt{-2\ln(1-z)}$. We thus arrive at the following table relating 1-, 2-, and 3-σ limits and $R$.

Table 2.1 Relations between 1-σ, 2-σ, and 3-σ limits and $R$.

| Limit | $Z$ (%) | $R$ |
|---|---|---|
| 1-σ | 68 | 1.51 |
| 2-σ | 95 | 2.45 |
| 3-σ | 99.7 | 3.41 |

From the table we arrive at the 99.7 percentile point for $R = 3.41\sigma$. This is close to the value of three we might have anticipated, showing that the $x$-$y$ distribution differs only slightly from the circular distribution, and the difference in distributions is not very important.

**Appendix 3**.

Measurements of the optical spectrum (see page 102 of Dylan Williams' laboratory notebook #4) and a reflectance curve for the optical antireflective coating on the back of the $LiTaO_3$ wafer supplied by the manufacturer.

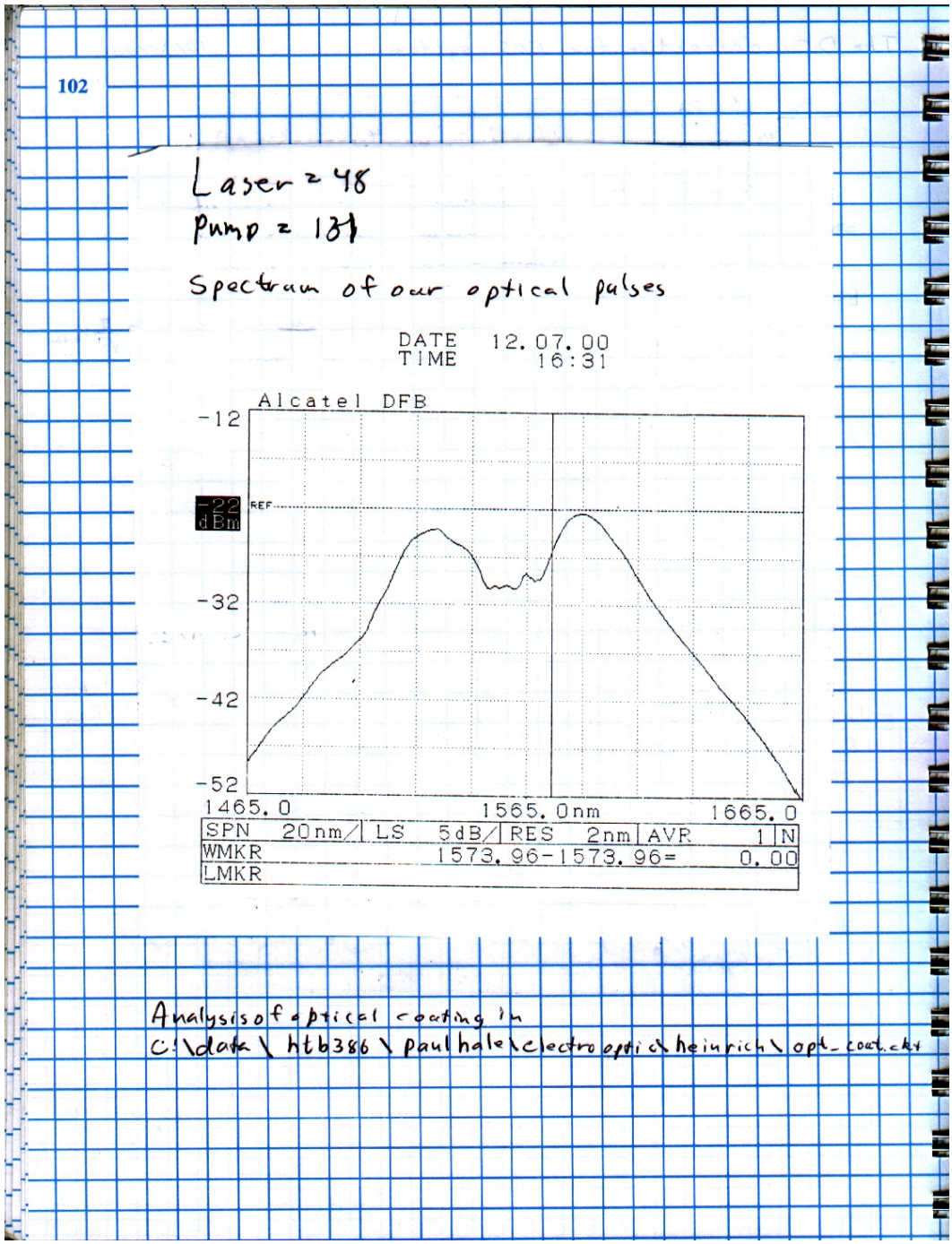
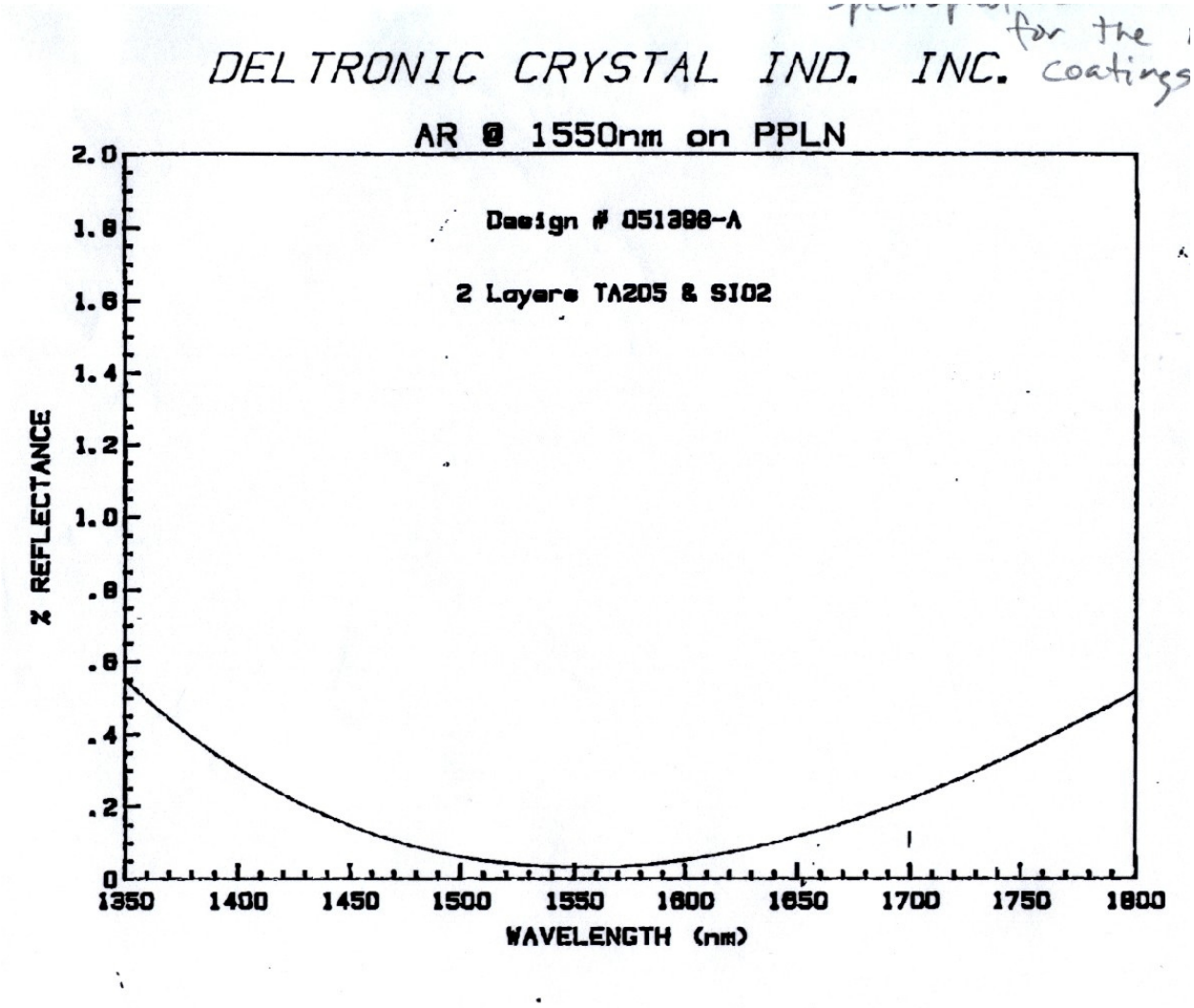
Data recieved from the manufacturer characterizing the antireflective optical coating they deposited on the back of the $LiTaO_3$ wafers.